東京大学 大学院 新領域創成科学研究科 物質系専攻 修士論文

Growth and characterization of Scandate insulator films for oxide field-effect devices

酸化物電界効果デバイスの作製に向けた スカンジウム酸化物絶縁膜の成長と評価

指導教員: Mikk Lippmaa 助教授

46111

Takayuki Uozumi

2006年1月31日

Contents

1 Introduction

1.1 Introduction

1.1.1 Transition metal oxides

Perovskite-type transition metal oxides (TMOs) provide a stage for strongly-correlated electrons to exhibit a rich repertoire of interesting phenomena. Most compounds with the general formula ABO_3 have the perovskite structure. As shown in Fig. 1, the unit cell of ABO_3 is represented by the A-site ions at the body center and the B-site ions at the corners. Oxygens form octahedra, surrounding the B-site ions. In perovskite-type oxides, the A-site cation is coordinated with twelve oxygen ions, and the B-site cation with six. Thus the ionic radius of the A cation is normally found to be slightly larger than that of the B cation. Therefore, the largest number of perovskite-type compounds are described by general formula $A^{+2}B^{+4}O_3$, where the A^{+2} cations are alkaline-earth ions, cadmium, lead, etc., while the B^{+4} cations are transition metals and some rare-earth ions, which are, in general, smaller than the cations of the A site. Diagrammatic presentations of the crystal symmetries and structures with respect to the ionic radii of the A and B cations for $A^{+2}B^{+4}O_3$ type compounds as well as the $A^{+3}B^{+3}O_3$ are shown in Fig.2(a) and (b), respectively [1].

The BO_6 octahedron in a perovskite oxide ABO_3 forms a three-dimensional network, so that, if the system is metallic, electric conduction is three-dimensional along the BO_6 network. The most important advantage of the perovskite structure is that the BO_6 network is stable against substitutions of the A-site ion. Therefore, perovskite oxides ABO_3, with B of a TM cation, provide us with an ideal setting to study electron correlations. With this advantage, we can employ three important strategies

1. Filling control: The nominal number of conduction electrons per unit formula is controlled by chemical substitution of an A ion for that of an ion with a different valence.

2. Bandwidth control: the B-O-B bond angle can be changed by changing the ionic radius of the A-site ion. The bond-angle buckling is governed by the so-called tolerance factor. The buckling of the B-O-B bond angle reduces the bandwidth (W), since the effective d-electron transfer interaction between the neighboring B sites is governed by a transfer process via the O $2p$ states. Thus the ratio of the Coulomb interaction U to W (U is assumed to be insensitive to substitutions) can be systematically controlled.

3. Dimension control: By changing the crystal structure from the simple perovskite to

a layered perovskite, such as A_2BO_4, we can follow how the electronic states change by reducing the network paths of the system.

These principles guide systematic research of the perovskite TMOs, hence the materials have been favored for investigating strong correlation effects.

Perovskite TMOs show various interesting physical properties in different material systems, such as, ferromagnetism and antiferromagnetism, conductors (including superconductor) and insulators, ferroelectrics and paraelectrics, and so on. Cuprates exhibiting high-Tc superconductivity [2], manganites with colossal magenetoresistance [3], and titanates with high dielectric constants [4] are among the most interesting properties related to perovskite TMOs.

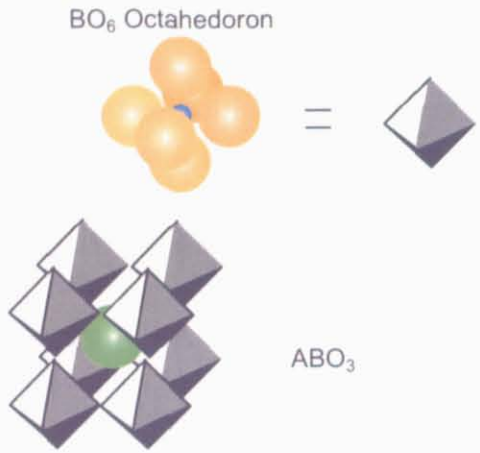

Figure 1: Schematic drawing of the perovskite structure, ABO_3.

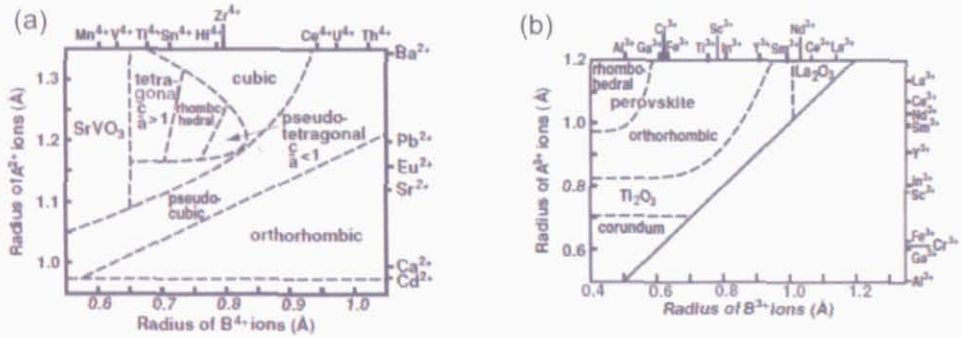

Figure 2: Classification of crystal structures for the (a) $A^{+2}B^{+4}O_3$ type compounds and (b) $A^{+3}B^{+3}O_3$ type compounds [1].

1.1.2 Electric field effect

A field-effect transistor (FET) basically consists of two parts, a semiconducting channel layer and a gate insulator layer. This device works by modulating the electrical carrier density, and hence the electrical resistance, of a thin semiconducting channel through the application of an electric field on the gate insulator. The transistor action is sensitive to the electronic states at the channel / insulator heterointerface.

Si-based FETs are widely used in all modern electronic applications, including cars, computers, mobile phones, kitchen appliances, etc.

This remarkably simple and very successful principle provides new opportunities for basic science and innovative device applications when applied to novel correlated electron systems whose properties depend strongly on the carrier concentration.

1.1.3 $SrTiO_3$

$SrTiO_3$ (Strontium titanate, STO) is a band insulator ($E_{gap} \approx 3.2$ eV[5]) with a cubic perovskite structure. The lattice constant is 3.905 Å [6]. It has long been studied for its unique dielectric properties, i.e., its very large dielectric constant, which increases from about 300 at room temperature to more than 10000 at low temperature [4]. In its pure, unstressed form, STO is an incipient ferroelectric, remaining paraelectric down to 0 K in a so-called quantum paraelectric state. Isotopic substitution [7], application of an electric field [8], or application of stress [9], can easily disturb this state, resulting in ferroelectricity. Room-temperature ferroelectricity in strained STO epitaxial films grown on a $DyScO_3$ (110) single crystal substrate has been recently reported [10].

The Fermi level of STO is located close to the conduction band bottom and it is easy to induce metallic conductivity by cation substitution or introduction of oxygen deficiency at a fairly low carrier density of about 10^{18} cm^{-3} [11]. The mobility of metallic STO increases with decreasing temperature [11]. Superconductivity appears at a carrier concentration range of 10^{19}-10^{21} cm^{-3}[12].

Atomically flat STO (100) single crystal substrates with single unit cell steps can be obtained by treating the crystal surface with a pH-controlled NH_4F-HF solution [13].

It has been a material of widespread interest in the world of oxide electronics and it is often integrated into epitaxial oxide heterostructures. Many examples of prototypes of electronic devices based on the exotic properties of perovskite oxides already exist. Arguably, it can be said that STO is among the most used materials in these oxide heterostructures, for instance, field-effect transistors [14, 15, 16, 17, 18, 10, 20, 21], Photodiodes [22], p-i-n diodes [23], nonvolatile memories [24], PCI (photocarrier injection) [25, 26], etc.

1.2 Purpose of this study

The purpose of this study is to develop $SrTiO_3$-based field-effects transistors with improved low-temperature performance. $SrTiO_3$-based FETs have already been fabricated and studied using amorphous and an epitaxial wide-gap insulator $CaHfO_3$. Unfortunately, epitaxial $CaHfO_3$ films with sufficient thickness could not be grown with atomically flat surfaces due to a lattice mismatch with the $SrTiO_3$ substrate. Relatively thick epitaxial insulator films are required to obtained fully epitaxial field-effect devices. Thus, wide-gap insulators that have smaller mismatch with $SrTiO_3$ than $CaHfO_3$ were explored in this work. The growth of insulator films and integration of such films in device structures was the main focus of this study.

1.3 Outline of the thesis

This thesis mainly describes insulating oxide thin films growth and characterization, and the examination of these films as gate insulators for $SrTiO_3$-based field-effect transistors. Chapter 2 introduces the thin film fabrication and characterization system in detail. An attempt was made to detect and characterize relatively low-energy and low-density interface statess in order to improve the performance of amorphous $CaHfO_3$ / $SrTiO_3$ field-effect transistors, as described in Chapter 3. In Chapter 4, the growth and characterization of wide-gap insulators is described. The fabrication of $SrTiO_3$ based field-effect transistors using wide-gap insulators is introduced in Chapter 4 and details are presented in Chapter 5. The evaluation of the performance of these field-effect transistors is also discussed.

References

[1] I.H.Inoue

Electrostatic carrier doping to perovskite transition-metal oxides

Semicond. Sci. Technol. 20, S112 (2005)

[2] J.G.Bednorz, A.Müller

Possible highTc superconductivity in the Ba-La-Cu-O system

Z. Phys. B. 64, 189 (1986)

[3] Y.Tomioka, A.Asamitsu, H.Kuwahara, Y.Moritomo, Y.Tokura

Magnetic-field-induced metal-insulator phenomena in $Pr_{1-x}Ca_xMnO_3$ with controlled charge-ordering instability

Phys. Rev. B. 53, R1689 (1996)

[4] T.Sakudo, H.Unoki

Dielectric Properties of $SrTiO_3$ at low temperature

Phys. Rev. Lett. 26, 851 (1971)

[5] M.Cardona

Optical Properties and Band Structure of $SrTiO_3$ and $BaTiO_3$

Phys.Rev. 140, A651 (1965)

[6] K.H.Hellwege, A.M.Hellwege (eds)

Landolt-Börnstein:Numerical Data and Functional Relationships in Science and Technology New Series, Group III, Vol.16a, 59-64 (Springer, Berlin, 1981).

[7] M.Itoh, R.Wang, Y.Inaguma, T.Yamaguchi, Y-J.Shan, T.Nakamura

Ferroelectricity Induced by Oxygen Isotope Exchange in Strontium Titanate Perovskite

Phys. Rev. Lett. 82, 3540 (1999)

[8] J.Hamberger, P.Lunkenheimer, R.Viana, R.Böhmer, A.Loidl

Electric-field dependent dielectric constant and nonlinear susceptibility in $SrTiO_3$

Phys. Rev. B. 52, 13159 (1995)

[9] H.Uwe, T.Sakudo

Stress-induced ferroelectricity and soft phonon modes in $SrTiO_3$

Phys. Rev. B. 13, 271 (1976)

[10] J.H.Hanei, P.Irvin, W.Chang, R.Uecker, P.Reiche, Y.L.Li, S.Choudhury, W.Tian, M.E.Hawley, B.Craigo, A.K.Tagantsev, X.Q.Pan, S.K.Streiffer, L.Q.Chen, S.W.Kirchoefer, J.Levy, D.G.Shlom

Room-temperature ferroelectricity in strained $SrTiO_3$

Nature 430, 758 (2004)

[11] O.N.Tufte, P.W.Chapman

Electron Mobility in Semiconducting Strontium Titanate

Phys. Rev. 155, 796 (1967)

[12] J.F.Schooley, H.P.R.Frederikse, W.R.Hosler, E.R.Pfeiffer

Superconducting Properties of Ceramic Mixed Titanates

Phys. Rev. 159, 301 (1967)

[13] M.Kawasaki, K.Takahashi, T.Maeda, R.Tsuchiya, M.Shinohara, O.Ishiyama, T.Yonezawa, M.Yoshimoto,H.Koinuma

Atomic Control of the $SrTiO_3$ Crystal Surface

Science 266, 1540 (1994)

[14] E.Bellingeri, L.Pellegrino, D.Marré, I.Pallecchi, and A.S.Siri

All-$SrTiO_3$ field effect devices made by anodic oxidation of epitaxial semiconducting thin films

J. Appl. Phys. 94, 5976 (2003)

[15] F.Pan, D.Olaya, J.C.Price, C.T.Rogers

Thin-film field-effect transistors based on La-doped $SrTiO_3$ heterostructures

Appl. Phys. Lett. 84, 1573 (2004)

[16] K.Shibuya, T.Ohnishi, M.Lippmaa, M.Kawasaki, H.Koinuma

Single crystal $SrTiO_3$ field-effect transistor with an atomically flat amorphous $CaHfO_3$ gate insulator

Appl. Phys. Lett. 85, 425 (2004)

[17] K.Shibuya, T.Ohnishi, T.Uozumi, T.Sato, M.Lippmaa, M.Kawasaki, H.Koinuma

Field-effect modulation of the transport properties of nondoped $SrTiO_3$

Appl. Phys. Lett. Submitted

[18] J.A.Misewich, A.G.Schrott

Room-temperature oxide field-effect transistor with buried channel

Appl. Phys. Lett. 76, 3632 (2000)

[19] K.Ueno, I.H.Inoue, H.Akho, M.Kawasaki, Y.Tokura, H.Takagi

Field-effect transistor on $SrTiO_3$ with sputtered Al_2O_3 gate insulator

Appl. Phys. Lett. 83, 1755 (2003)

[20] K.S.Takahashi, D.Matthey, D.Jaccard, J.-M.Triscon, K.Shibuya, T.Ohnishi, M.Lippmaa

Electrostatic modulation of the electronic properties of Nb-doped $SrTiO_3$ superconducting film

Appl. Phys. Lett. 84, 1722 (2004)

[21] D.Matthey, S.Gariglio, J.-M.Triscone

Field-effect experiments in $NbBa_2Cu_3O_{7-\delta}$ ultrathin films using a $SrTiO_3$ single-crystal gate insulator

Appl. Phys. Lett. 83, 3758 (2003)

[22] Y.Watanabe, M.Okano

Photodiode properties of epitaxial $Pb(Ti,Zr)O_3/SrTiO_3$ ferroelectric heterostructures

Appl. Phys. Lett. 78, 1906 (2001)

[23] M.Sugiura, K.Uragou, M.Tachiki, T.Kobayashi

Estimation of trap levels in $SrTiO_3$ epitaxial films from measurement of $(LaSr)MnO_3/SrTiO_3/(LaSr)TiO_3$ p-i-n diode characteristics

J. Appl. Phys. 90, 187 (2001)

[24] Y.Watanabe, J.G.Bednorz, A.Bietsch, Ch.Gerber, D.Widmer, A.Beck, S.J.Wind

Current-driven insulator-conductor transition and nonvolatile memory in cheomium-doped $SrTiO_3$ single crystal

Appl. Phys. Lett. 78, 3738 (2001)

[25] T.Muramathu, Y.Muraoka, Z.Hiroi

Photocarrier Injection and Current-Voltage Characteristics of $La_{0.8}Sr_{0.2}MnO_3/SrTiO_3$:Nb Heterojunction at Low Temperature

Jpn. J. Appl. Phys. 44, 7367 (2005)

[26] H.Katsu, H.Tanaka, T.Kawai

Dependence of carrier doping level on the photo control of (La, Sr)$MnO_3/SrTiO_3$ functional heterojunction

J. Appl. Phys. 90, 4578 (2001)

2 Fabrication and characterization techniques of oxide thin films

2.1 Pulsed laser deposition (PLD)

Pulsed laser deposition (PLD) is widely used for oxide thin film fabrication and one of the best methods to obtain high-quality oxide thin films.

In the present work, a KrF excimer laser (Lambda-Physik Compex 102) was used for ablating ceramic targets. The laser can deliver up to 350 mJ in a 20 ns pulse at a wavelength of 248 nm. Light from the laser was directed into the vacuum chamber with a single mirror. Low-energy edges of the beam through an optical variable attenuator synthetic quartz window. A single focusing lens at the target surface

In laser ablation, high-energy pulse lasers, such as excimer and Nd:YAG lasers are typically used to evaporate material from a target surface. Firing a high-power nanosecond-scale laser pulse on a target results in near-instantaneous heating of a thin surface layer to temperatures where a plasma is formed. The plasma expands rapidly, carrying material from the ablation target to a film surface. As a result of ablation, ions, atoms, and clusters may be deposited at the surface. Crystal growth is possible due to the high kinetic energy of the ablated species, often helped by a high substrate temperature.

In the case of film growth by resistance heating of evaporation sources, the rate of evaporated for each components can not be controlled easily due to the difference of vapor pressure of each element. On the other hand, pulsed heating of an ablation target surface with a high-energy laser pulse creates temperatures that are high enough for all elements to be removed from the target surface with equal probability. This means that the transfer of material from a target to a film is stoichiometric. This makes the laser ablation technique very suitable for the growth of oxide materials, because the stoichiometry of the film can be controlled by preparing a ceramic target with the desired composition. This is generally much easier to do using conventional powder ceramic techniques than it would be by attempting to control evaporation rates of multiple elements simultaneously in a vacuum system. Another advantage of laser ablation for oxide film growth is the ability to process materials with very high melting points. Moreover, PLD is not sensitive to the background gas pressure, because the energy required to vaporize the solid target material is introduced from outside of the deposition chamber. Background gas pressures can vary from ultra-high vacuum to approximately 1 Torr. For oxide thin film fabrication, the use of an oxygen ambient is important in order to avoid the creation of oxygen deficiency. If the background oxygen pressure is below about 500 mTorr, it also possible to use reflection high-energy electron diffraction (RHEED) for in situ and real-time monitoring of crystal growth.

The main weaknesses of PLD are the difficulty of fabricating homogeneous film over a large area, and a general lack of repeatability, mainly due to the difficulty of controlling the spacial characteristics of the pulse laser beam[1].

The homogeneity of films grown by PLD depends on the ablation plume radius and a typical homogeneous deposition area is limited to less than 1 cm^2. These days, there is considerable effort to understand the effects of the various hidden process parameters on the quality of thin films, thereby improving the repeatability of PLD experiments[1].

The deposition system used in this study[2] consists of two parts: a load lock and the main deposition chamber (Fig. 3). The deposition chamber is pumped by two turbomolecular vacuum pumps (TMP). The background vacuum level of the system is $\approx 2\times10^{-9}$ Torr. For the ablation of targets, a KrF excimer laser (λ = 248 nm, COMPEX 102, Lambda Physik) was used. The pulsed laser beam with a pulse width of 20 ns was introduced into the chamber through a synthetic quartz window and focused onto a target surface. The energy density of the laser at the target surface was controlled by changing the high voltage of the excimer laser or by inserting an optical variable attenuator in the beam path. This was necessary because changing the laser pulse energy by adjusting the high voltage of the excimer laser, also results in a change of the laser beam divergence. A divergence change alters the width of the laser beam on the target surface, changing the energy density. An optical attenuator can be used to control the pulse energy while the laser discharge parameters are held constant. In this case there is no change in the optical characteristics of the laser beam and the enegy density can be controlled more accurately. The attenuator used in this study was self built and allowed the laser eneregy to be cut by 5 to 95%.

Up to four ablation targets could be mounted on a target carrousel inside the chamber. Additional targets could be loaded through the load-lock chamber without breaking the vacuum of the main chamber. To avoid surface erosion, the targets were continouously rotated with a variable-speed motor during laser firing.

The crystallinity of oxide thin films is very sensitive to the growth temperature. In this chamber, a Nd:YAG laser (λ = 1064 nm, NEC SL117) was used for substrate heating, allowing the growth temperature to reach $\approx$ 1400°C. The substrate temperature was monitored with an optical pyrometer operating at 2 μm.

As shown in Fig. 4, the substrates were clamped on a stainless steel sample holder. The sample stack on the sample holder consisted of a sapphire sheet that served as a mechanical support. A 0.05 mm-thick oxidized nickel sheet was mounted on the sapphire sheet. This sheet served as an absorber for the infrared light from the Nd:YAG heating laser. Substrates were mounted on top of this nickel sheet. Several thin metal foils were inserted between the heat-absorbing nickel sheet and the substrate crystal. Typically three foils in a Au (0.01 mm)/Ni (0.005 mm)/Au (0.01 mm) configuration were used.

The substrate-target distance was usually about 50 mm, but easily tunable. A movable mask could be moved in front of the sample with a computer-controlled stepping motor. The background oxygen gas was introduced into the chamber with a manual molecular leak valve and the gas flow was directed at the sample surface with a nozzle.

Most of the growth parameters, such as the substrate temperature, pulse number and pulse rate of the KrF excimer laser, etc. were controlled with a computer running a control program under LabVIEW (National Instruments). The front panel of the control system is shown in Fig. 5.

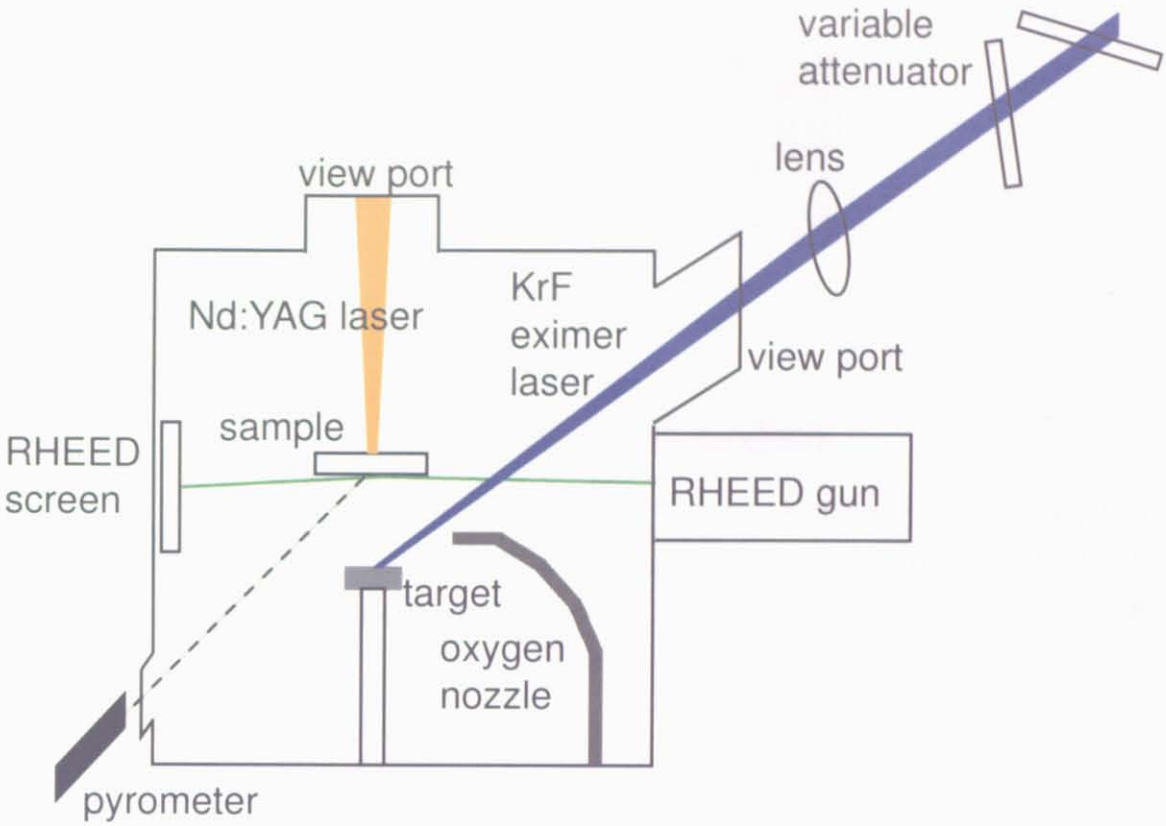

Figure 3: Schematic view of the PLD chamber.

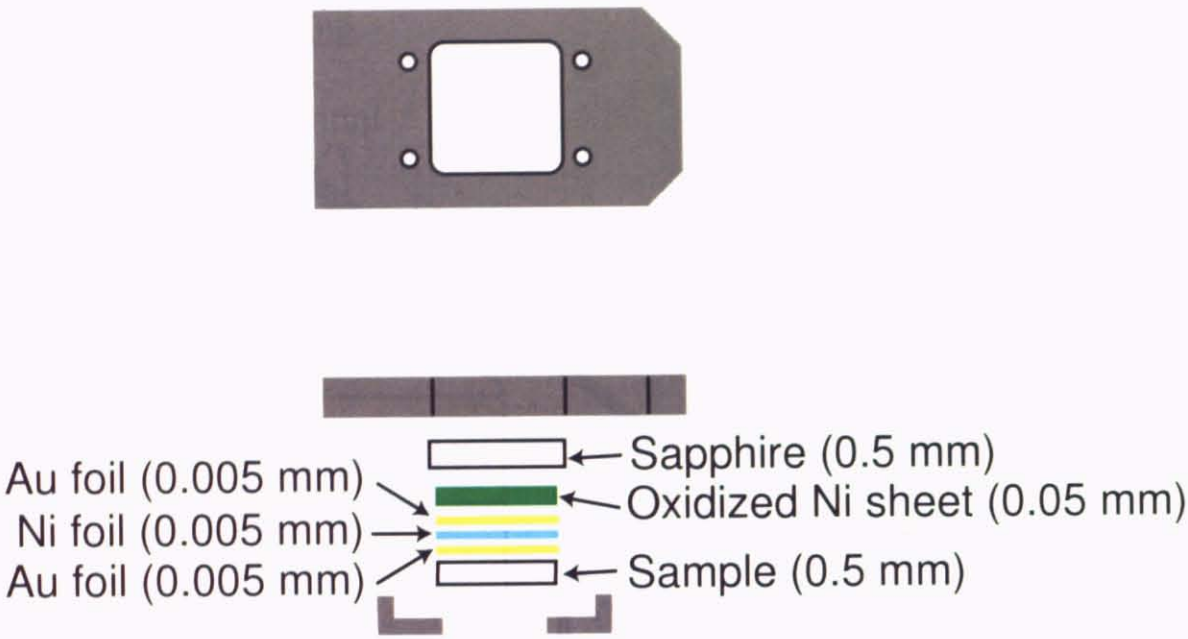

Figure 4: Schematic view of the sample holder.

Figure 5: Image of the LabVIEW control panel.

2.2 Reflection high energy electron diffraction (RHEED)

Electron diffraction has been widely used for monitoring surface structures and film growth of various semiconductors. RHEED can be easily integrated in a PLD system due to the grazing-incidence diffraction configuration. It is a powerful technique for studying surface structures of flat surfaces.

RHEED works by directing an accelerated electron beam (10 to 30 keV) at a crystal surface at a low incident angle (3 to 5°). The high-energy electrons strongly interact with the sample surface and because of the glancing angle of incidence, only a few topmost atomic layers are probed. Therefore, RHEED is sensitive to surface structures.

The intensity of the specular reflection beam depends on the surface roughness, and observation of this intensity gives real-time information of film growth dynamics. From the behavior of the specular reflection intensity, the crystal growth mode can be decided, whether it is layer-by-layer or step-flow mode. If the substrate surface is atomically flat before film growth, the diffracted beam has the highest intensity. At the initial stage of layer-by-layer growth of a thin film, the specular intensity drops due to scattering by increased surface roughness. When the density of step edges reaches a maximum at approximately 0.5 monolayer coverage, the scattering is the largest and the intensity of specular reflection is at its weakest. After that, the remaining holes in the surface terraces are gradually filled and the reflected electron beam intensity gradually recovers. Finally, as a monolayer is completed, the intensity recovers close to its original value. The deposition rate can be decided from the period of this oscillation. A schematic view of layer-by-layer mode growth is shown in Fig. 6.

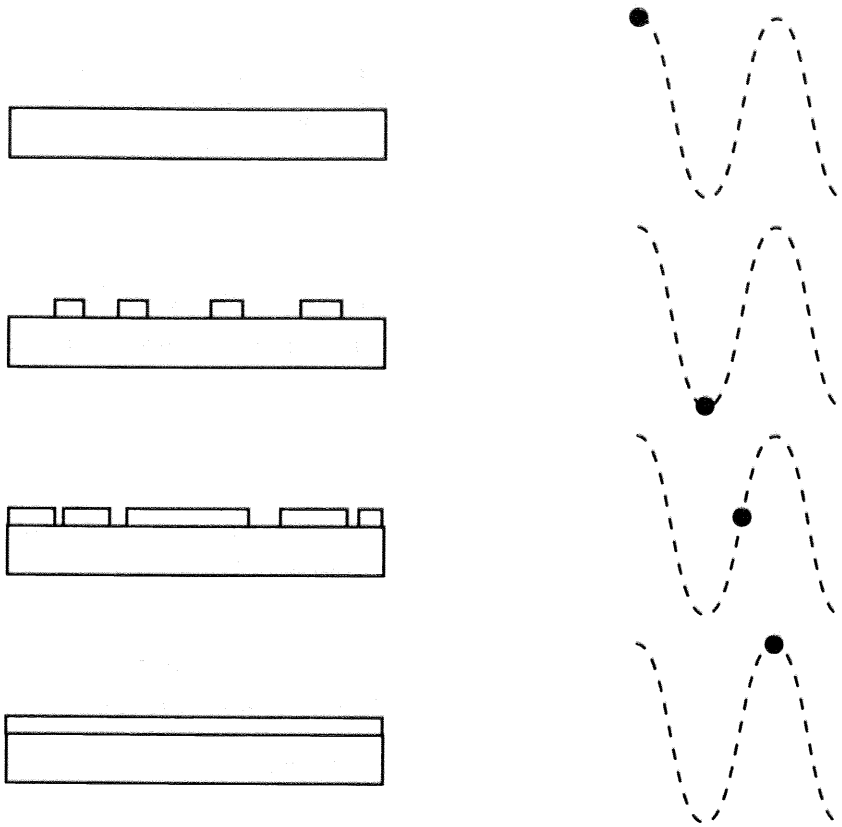

Figure 6: Illustration of the layer-by-layer mode and the corresponding RHEED oscillation.

2.3 Atomic force microscopy (AFM)

An atomic force microscope (AFM) is a scanning probe microscope that can be used to obtain surface morphology images of samples. Height information is obtained in an AFM by raster-scanning a probe needle over a rectangular area of the surface. The basic building blocks of a typical AFM are shown in Fig. 7.

The needle that probes the surface is attached to a flexible cantilever. Several different measurement modes can be used to obtain a surface morphology image. In this study, the dynamic force mode (DFM) was used. In DFM mode, a needle is placed on flexible cantilever and the cantilever is vibrated by an external force. As a needle approaches to the sample surface, the amplitude of the cantilever vibration decreases due to the interaction between the needle and the sample surface. The actual tip vibration amplitude is measured with a segmented photo detector. By adjusting the tip height during a scan so that there is no loss of vibration amplitude, a topographic image can be obtained. The resolution of the system is determined by the diameter of the tip and it is routinely possible to achieve nm order spatial resolution. An advantage of this technique over scanning tunneling microscopy, for example, is that AFM is not limited by the conductivity of the sample, and can be used in air, in liquids, or in vacuum. In this study, Nanopics 1000 and SPI3800N with SPA400 (Seiko Instruments) microscopes were used.

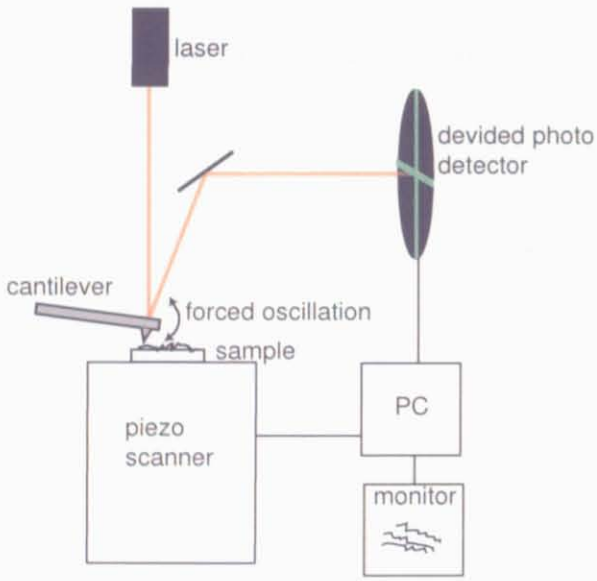

Figure 7: Schematic image of AFM operation.

2.4 X-ray Diffraction (XRD)

X-ray diffraction (XRD) is traditionally used to study the crystal structure and crystallinity of materials. Conventional powder-type diffractometers are technically the most simple but can only be used to determine the out of plane lattice parameter of thin films. The latice parameter of a film can be determined by measuring the diffraction angle of a film peak in a $2\theta/\theta$ diffraction pattern and calculating the atomic spacing with Bragg's law,

$$2d_{\mathrm{hkl}} \sin\theta = n\lambda, \tag{1}$$

where λ is the x-ray wavelength and n is an integer giving the diffraction order.

The full width at half maximum obtained by a θ scan is a good indication of the mosaicness of a lattice and is thus a good measure of crystallinity of a film. A schematic view of the XRD system used in this work is shown in Fig. 8. All measurements were performed with a conventional M03-X-HF22 powder XRD system (MacScience). The x-ray source was a Cu tube.

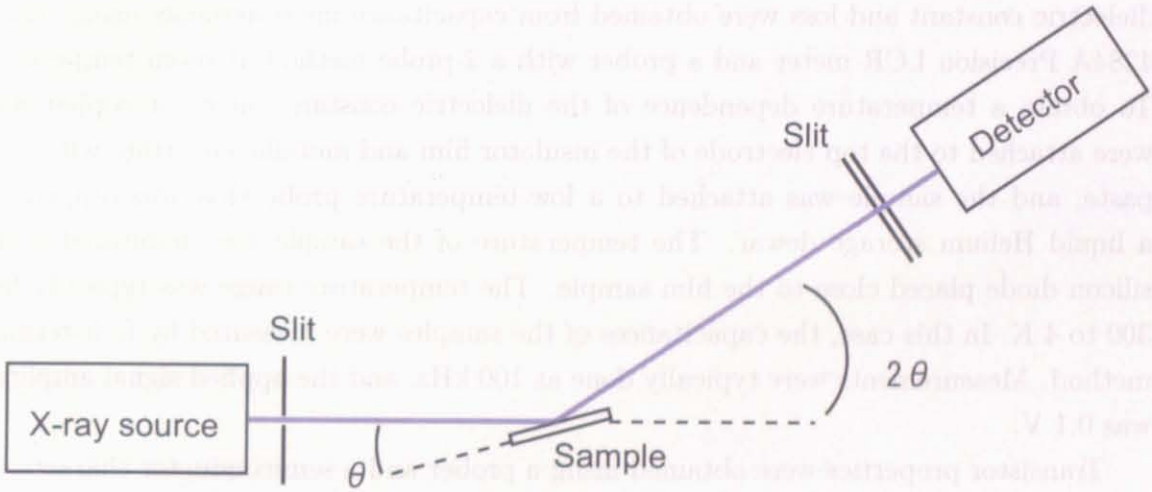

Figure 8: Schematic view of the x-ray diffraction system.

2.5 Electrical measurement

The insulating properties, breakdown field, and dielectric constant of insulating films were studied in this work. In some cases, complete field-effect transistors were fabricating, integrating the insulator films. In those cases the switching characteristics of the transistors were measured as well.

To determine the breakdown field of insulator films, samples were grown on conducting 0.5wt% Nb-doped STO (100) single crystal substrates. After film growth, $\phi = 0.2$ mm Al electrodes were evaporated on the film surface. A typical number of surface electrodes was on the order of 100. The breakdown field measurements were done with a KEITHLEY 4200 semiconductor characterization system while contact with individual pads was made in a manual room-temperature probing station (OYAMA CO,.LTD). The values of breakdown fields were calculated from the bias voltage where mechanical breakdown happened.

The dielectric characterization was done with similar samples. However, to obtain accurate capacitance values, larger area (0.6 $\times$ 0.6 mm) top electrodes were used. The dielectric constant and loss were obtained from capacitance measurements using Agilent 4284A Precision LCR meter and a prober with a 2-probe method at room temperature. To obtain a temperature dependence of the dielectric constant, silver or copper wires were attached to the top electrode of the insulator film and metallic substrate with silver paste, and the sample was attached to a low-temperature probe that was dipped into a liquid Helium storage dewar. The temperature of the sample was monitored with a silicon diode placed close to the film sample. The temperature range was typically from 300 to 4 K. In this case, the capacitances of the samples were measured by four-terminal method. Measurements were typically done at 100 kHz, and the applied signal amplitude was 0.1 V.

Transistor properties were obtained using a prober and a semiconductor characterization system at room temperature. Low-temperature measurements were performed in a flow-type Helium cryostat.

2.6 Optical measurement

Optical measurements were done to determine the optical band gap of the insulator films. The transmittance of insulator films on Al_2O_3 was measured with a JASCO V570 UV-VIS-NIR spectrometer (Fig. 9). The samples used in optical measurements were grown at room temperature in amorphous form on Al_2O_3 substrates. There should be no major difference between the values obtained from amorphous and epitaxial films. From transmittance measurement, the absorption and reflectivity could be calculated.

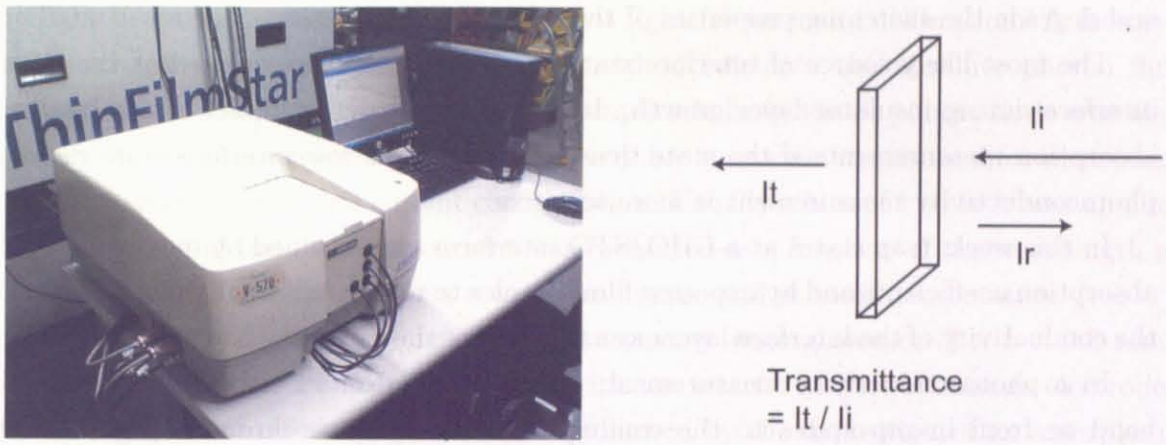

Figure 9: A picture of JASCO V570 UV-VIS-NIR spectrometer, and a schematic view of the transmittance measurement

References

[1] T.Ohnishi, M.Lippmaa, T.Yamamoto, S.Megro, H.Koinuma

Improved stoichiometry and misfit control in perovskite thin film formation at a critical fluence by pulsed laser deposition

Appl.Phys.Lett., 87, 241919 (2005)

[2] S.Ohashi, M.Lippmaa, N.Nakagawa, H.Nagasawa, H.Koinuma, M.Kawasaki

Compact laser molecular beam epitaxy system using laser heating of substrate for oxide film growth

Rev.Sci.Instrum., 70, 178 (1999)

3 Photoconductivity measurement

3.1 Introduction

It is known that the mobility of carriers in STO single crystals increases at lower temperatures [1]. Therefore, the transistor switching action can be expected to improve as the temperature is reduced. However, various STO-based transistors, especially those with amorphous gate insulators do not show a field-effect mobility increase upon cooling. One possible reason for this is the presence of interface states that suppress carrier mobility and degrade the switching properties of the field effect transistor.

The most likely source of interface states are defects that are created at the channel interface during insulator layer growth. It is possible to detect defect states by optical absorption measurements if the state density is high. For low interface state densities, photoconductivity measurement is more sensitive.

In this work, trap states at a-CHO/STO interfaces were studied by measuring optical absorption coefficients and by exposing film samples to monchromatic light and measuring the conductivity of the interface layers as a function of the wavelength of the incident light.

In a photoconductivity measurement, electrons are excited either from the valence band or from in-gap states to the conduction band by monochromatic light and the photo-induced carriers are detected by measuring the conductivity of the sample. This technique can be used even for very thin layers, such as interfaces that have a characteristic electronic thickness of only a few nanometers. Optical absorption would not be useful in such cases due to the small level of absorption in very thin layers.

Various interface structures were studied using photoconductivity measurements and attempts were made to extract characteristic in-gap state energies from the photoconductivity spectra.

3.2 Photoconductivity measurement system

A schematic view of the photoconductivity measurement system is shown in Fig. 10. A self-built system was used for the measurement. The light source was a 1 kW xenon lamp (Ushio short arc). Light from the lamp was focussed on the entrance slit of a double monchromator (JASCO CT-25D). The gratings allowed a wavelength range from 200 nm to approximately 700 nm to be covered. The monochromator wavelength was controlled via a GPIB bus from a measurement computer running a LabVIEW program. Light from the monochromator was focused on the sample surface. A quartz plate was placed in the light beam to extract some of the incident light for intensity calibration. A factory-calibrated Hamamatsu Si photodiode was used to calculate the absolute photon flux incident on the sample surface. The signal amplitude from the Si pohotodiode was also recorded by the measurement computer. A Keithley sourcemeter was used for measuring the sample conductivity in a 2-point configuration. Usually a bias of 1 to 10 V was applied to the sample and the resultant current was measured as a function of the wavelength of the incident light. All measurements were done in air and at room temperature

The samples for photoconductivity measurements were grown on $2 \times 5 \times 0.5$ mm^3 STO substrates. In order to make contact with the interface layer, aluminum electrodes were first deposited on clean STO surfaces, followed by the deposition of an amorphous CHO layer. The Aluminun electrodes configuration is shown in Fig.10. The samples were then mounted on a ceramic package and wire bonding was used to connect the aluminum electrodes of the sample to the contact pads of the ceramic chip carrier package. Connecting aluminum wires were bonded directly to the CHO film surface. The bonding force is sufficient to crush the thin insulator film and make contact with the aluminum electrodes at the substrate interface (Fig.10).

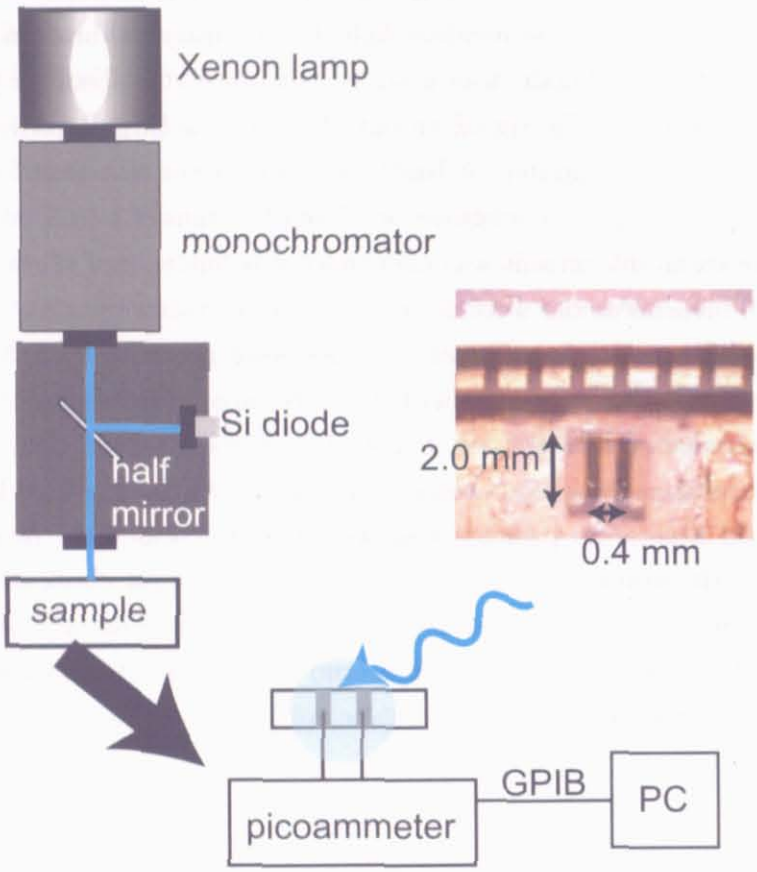

Figure 10: Schematic view of the photoconductivity measurement system. The photograph of typical sample is also shown. The Al electrodes were 0.4 mm × 2 mm.

The irradiated light at each wavelength from the Xenon lamp has a different intensity. Therefore, the measured photo-induced current has to be normalized by the intensity of the light at each wavelength. The intensity of light is proportional to the number of incident photons. The incident photon numbers were estimated as follows;

Si diode voltage: x [V]

Diode current conversion coefficient: 10^{-5} [A/V]

Light sensitivity of Si (Fig. 12(a)): $y(\lambda)$ [A/W]

Detected power: $\frac{x}{y10^5}$ [J/s]

Photon energy: $h\nu = \frac{hc}{\lambda}$ [J]

Detected photon flux: $\frac{x\lambda}{yhc10^5}$

Beam area: S' [m^2]

Sample area: S [m^2]

The intensity ratio of direct and reflected light (Fig. 12(b), (c)): d/r

Photon flux on sample: $\frac{d}{r}\frac{S}{S'}\frac{x\lambda}{yhc10^5}$

The number of photoinduced carriers: $n = \frac{I_{\text{photo}} - I_{\text{dark}}}{e}$

Photoconductivity: $\sigma = \frac{(I_{\text{photo}} - I_{\text{dark}})yhc10^5}{\lambda x(d/r)e}$

The procedure of photoconductivity measurement was as follows; The saturated photoinduced current at each wavelength was measured. Data was collected for 1000 seconds at each wavelength (Fig.11). The current values (Fig.13 (a)) at each wavelength were normalized by the photon flux using the light intensity number measured from the Si diode, as mentioned above. Typical photocurrent and normalized photoconductivity plots are shown in Fig. 13. As shown in Fig. 13(b), a peak was observed at around 2.3 eV, i.e. well below the band gap excitation energy. This peak suggests the existence of interface states at around 2.3 eV.

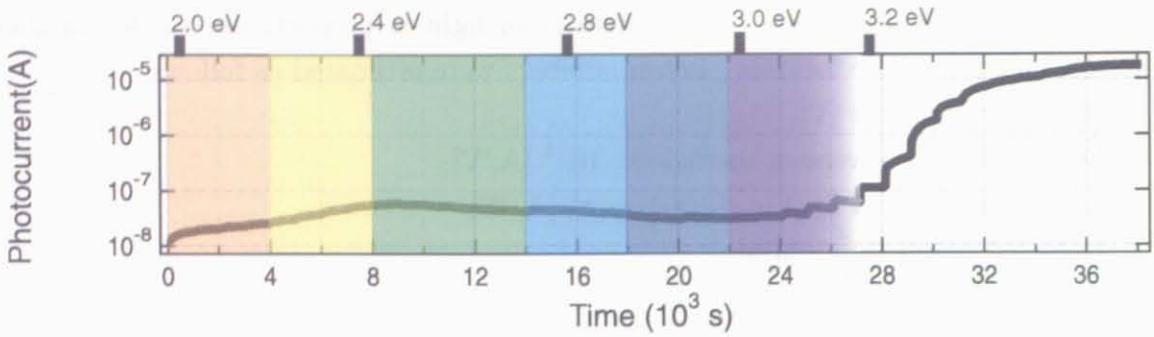

Figure 11: Photo-induced current at each wavelength. Measurements were done for 1000 seconds at each wavelength. The colors in figure indicates the wavelength of the visible light region.

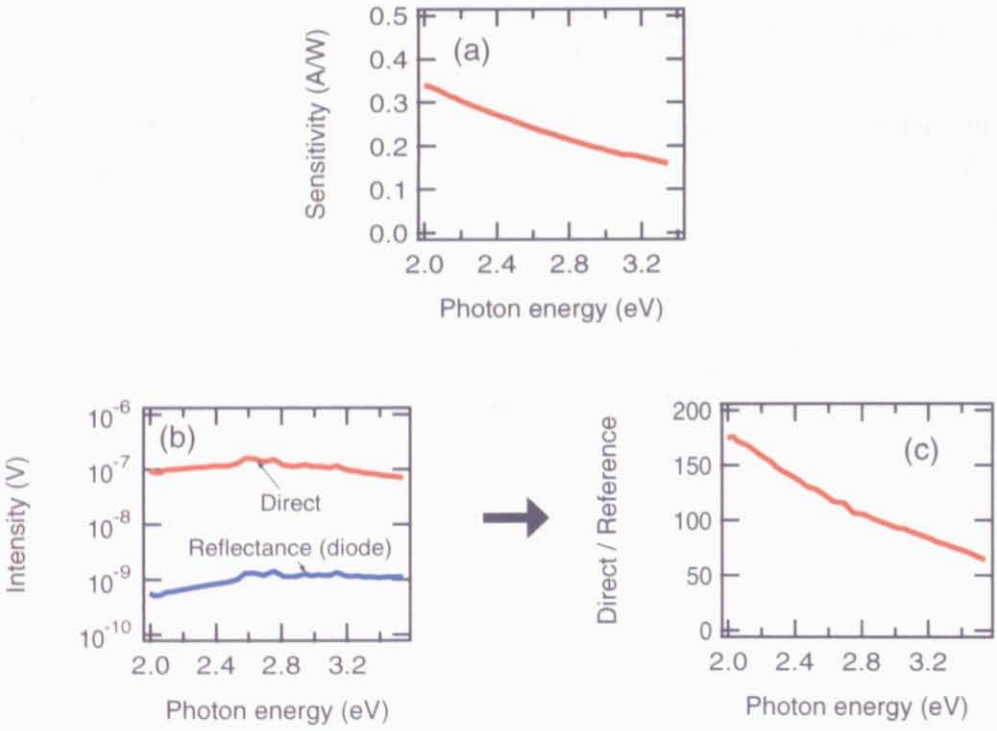

Figure 12: (a) The photo-sensitivity of Si diode. (b), (c) The intensity ratio of direct and reflectance light.

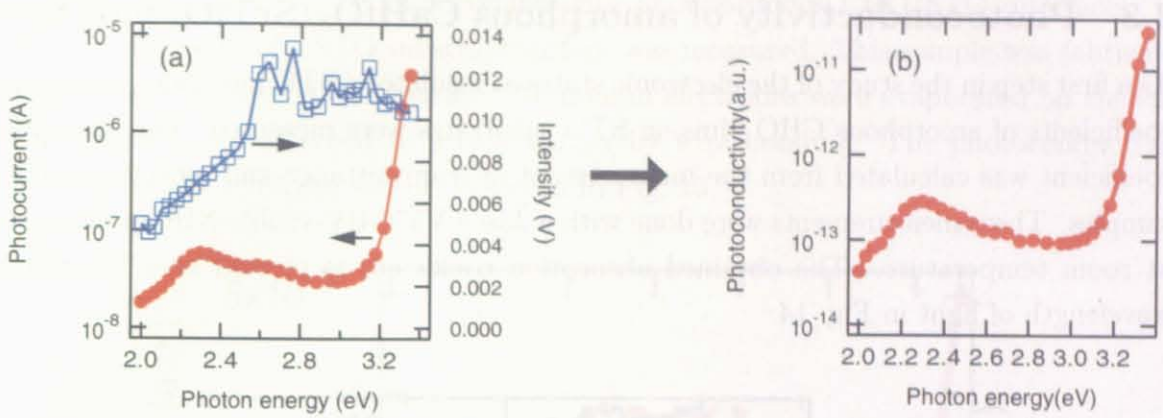

Figure 13: (a) Photo-induced current as a function of photon energy (filled circle). Intensity of light at each photon energy (open square). (b) Normalized photoconductivity (electrons per photon) as a function of photon energy.

3.3 Photoconductivity of amorphous $CaHfO_3/SrTiO_3$ interfaces

As a first step in the study of the electronic states at insulator / STO interfaces, absorption coefficients of amorphous CHO films on STO substrates were measured. The absorption coefficient was calculated from the measurement of transmittance and reflectivity of the samples. These measurements were done with a Jasco V570 UV-visible-NIR spectrometer at room temperature. The obtained absorption coefficient is plotted as a function of wavelength of light in Fig. 14.

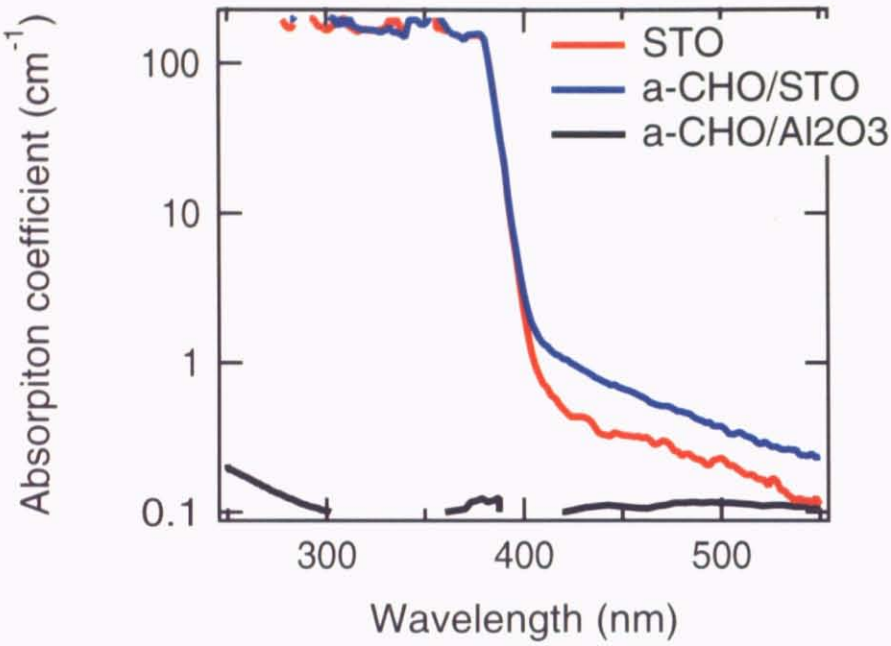

Figure 14: Absorption coefficient of amorphous CHO films on STO, a non-doped STO substrate, and amorphous CHO films grown on sapphire.

The band gap energy of STO is 3.2 eV [2]. As shown in Fig. 14, there is no obvious absorption peak in the STO band gap. It is hard to detect the presence of interface states in transmittance and reflectance measurements due to the small thickness of the interface layer compared with the bulk substrate crystal and the insulator film itself. For this reason, further effort was directed at detecting interface states by photoconductivity measurements.

Before measurement of photoconductivity at amorphous CHO/STO interfaces, the photoconductivity of a STO substrate surface was measured. This sample was fabricated using an as-supplied STO substrate. Aluminum electrodes were evaporated on the substrate surface and attached to a chip carrier by wire bonding. The photoconductivity spectrum of the reference sample is shown in Fig. 15.

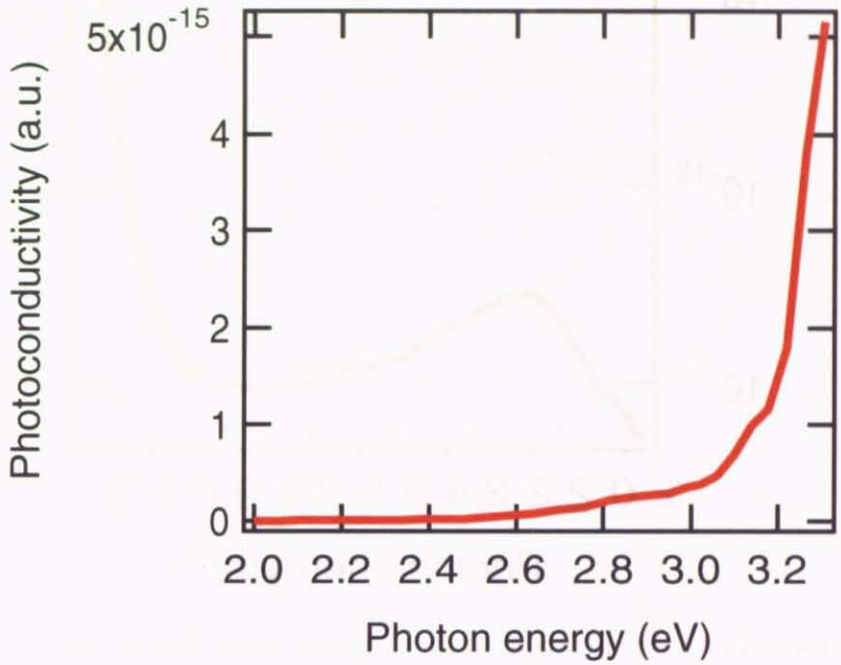

Figure 15: Photoconductivity spectrum of the STO substrate surface.

On the STO substrate surface, only the STO band gap excitation was observed above 3.2 eV. For comparison, a photoconductivity spectrum of an amorphous CHO/STO interface is shown in Fig. 16. The deposition conditions of the amorphous CHO film were as follows; oxygen partial pressure was 3 mTorr, pulse rate was 10 Hz, the laser fluence was 0.8 J/cm^2, giving a growth rate of 47 pulses per nominal CHO monolayer. This deposition rate is relatively high and significant plume sputtering of the interface layer can be expected under these film growth conditions.

As shown in Fig. 16, the photoconductivity of the amorphous CHO/STO interface has a strong peak at around 2.3 eV in addition to the band gap excitation at above 3.2 eV.

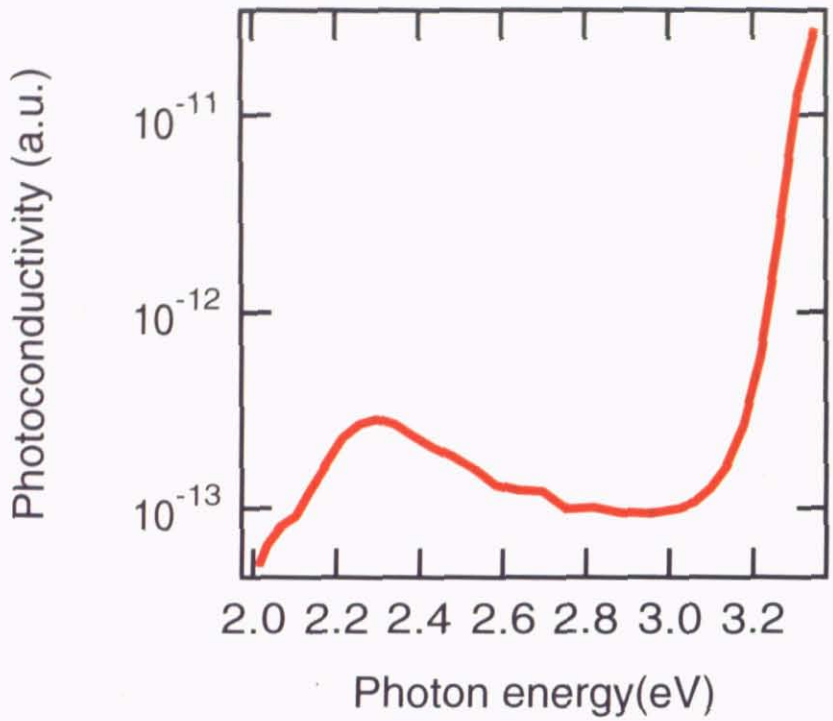

Figure 16: Photoconductivity spectrum of an as-grown amorphous CHO/STO interface.

The origin of this conductivity peak was studied further. For comparison with the samples grown on STO, amorphous CHO was deposited on $NdGaO_3$ single crystal substrates. This measurement was designed to answer the question whether the conductivity observed in CHO/STO samples is caused by a conducting layer in the CHO film or at the STO substrate surface.

Both CHO and NGO are wide-gap insulators [6, 7]. As shown in Fig. 17, the photoconductivity of CHO/NGO showed completely insulating behavior. From this result, it can be concluded that the photoconductivity did not originate in the amorphous CHO layer.

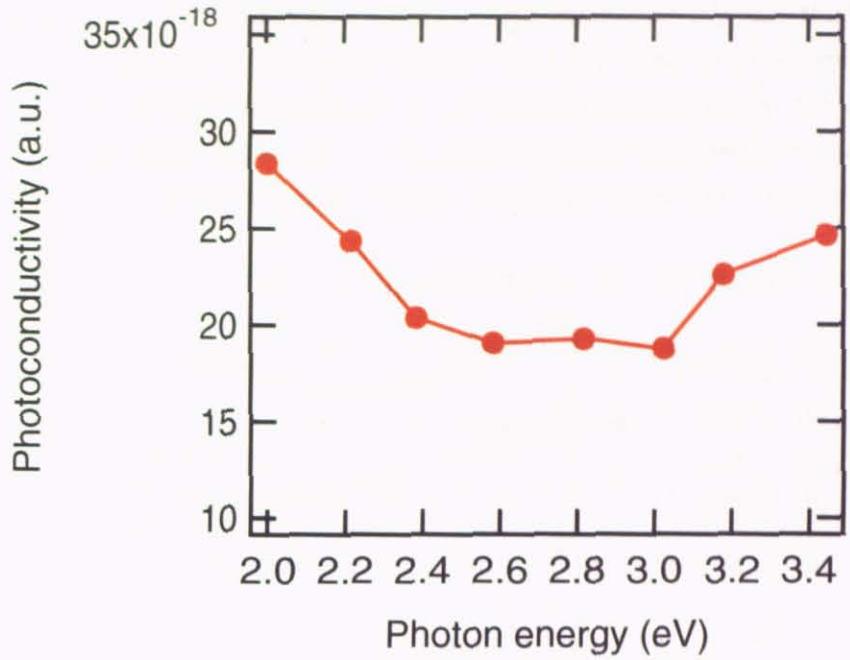

Figure 17: Photoconductivity of an amorphous CHO/NGO interface.

These results indicate that the photo-induced carriers were generated only at amorphous CHO/STO interfaces. It has been reported that there is a broad peak at around 2.4 eV in reduced STO bulk single crystals, using absorption coefficient measurements [5] and photoluminescence measurements[6]. Therefore, it can be concluded that oxygen vacancies due to the sputtering effect of ablation plume during insulator layer deposition creates oxygen vacancies in the surface layer of the STO substrate, resulting in the strong photoconductivity peak shown in Fig. 16.

To prove that oxygen vacancies are responsible for the interface conductivity, film samples were annealed in air. This treatment is known to be effective at refilling oxygen vacancies that are usually formed during high-temperature growth of oxide films at low background oxygen pressures. After annealing samples in air, photoconductivity spectra were measured again. The processing flowchart is outlined below:

- as-grown sample ⇒ photoconductivity measurement
- anneal in air at 150 °C ⇒ photoconductivity measurement
- anneal in air at 200 °C ⇒ photoconductivity measurement
- anneal in air at 250 °C ⇒ photoconductivity measurement
- anneal in air at 300 °C ⇒ photoconductivity measurement
- anneal in air at 350 °C ⇒ photoconductivity measurement

Interface current was measured in dark conditions after each annealing step. These current values at a bias of 10 V are plotted in Fig.18 as a function of annealing temperature.

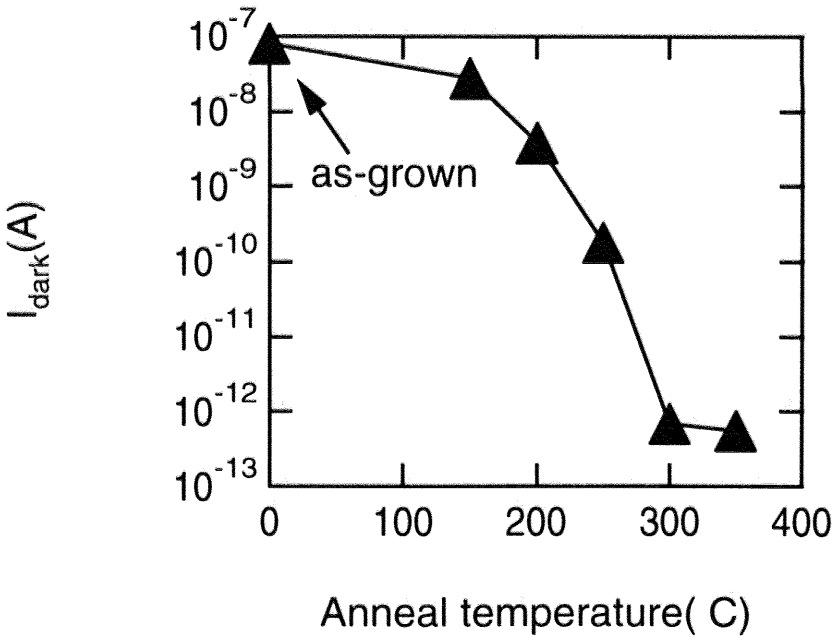

Figure 18: Interface current in dark conditions as a function of annealing temperature. Bias was 10 V.

As the annealing temperature increased, there was a clear drop in the current measured in dark conditions. This result indicates that the oxygen vacancies were filled by annealing treatment. The decrease of the dark current value saturated at above 300 °C, which means that all oxygen vacancies had been filled after annealing at that temperature. Changes in the photoconductivity spectra during the annealing treatment are shown in Fig. 19.

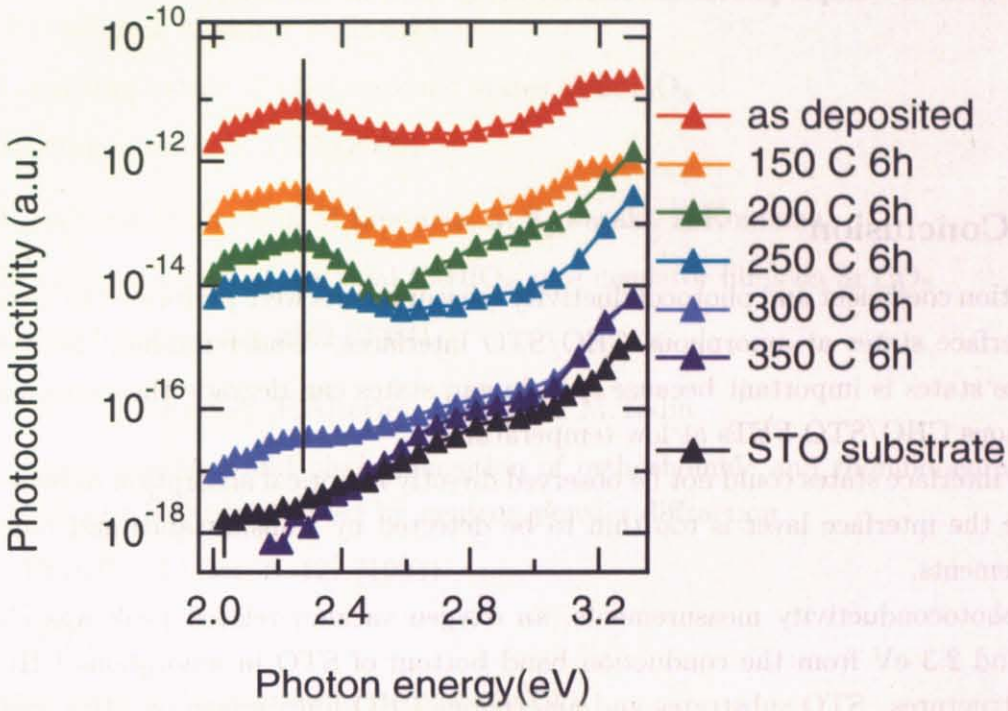

Figure 19: Effect of annealing CHO/STO films in air on the photoconductivity spectra.

The photoconductivity peak at around 2.3 eV could no longer be detected after the sample was annealed above 300 °C. Therefore, it can be concluded that the peak at 2.3 eV is indeed related to oxygen vacancies. This peak was not observed on original STO single crystal surfaces, and as mentioned above, amorphous CHO film itself did not respond to light illumination (Fig. 17). This result suggests that the oxygen vacancies were created by the sputtering effect of the PLD plume during insulator deposition. The oxygen vacancies could be removed by post-annealing the samples in air at 300 °C or higher.

However, transistors based on CHO / STO interfaces are always annealed after gate insulator deposition. The post annealing condition are: temperature 300 °C, time 6 hours. Therefore, the oxygen vacancies seen in these photoconductivity measurements can not be the cause for the observed degradation of FET performance at low temperature. It is likely that there are several types of vacancy defects in STO. Most of the defects, which give the 2.3 eV photoconductivity response, can be effectively removed by annealing the film in air.

This, however, does not rule out the possibility of other defect sites, possibly combined oxygen vacancy-cation defect clusters that may be responsible for shallow trapping levels close to the bottom of the conduction band in STO. Such shallow states can have a dramatic effect on the low-temperature performance of FET devices. However, such levels, located within $\sim$ 100 meV below the conduction band edge, are very difficult to observe with the simple photoconductivity setup used in this study.

3.4 Conclusion

Absorption coefficient and photoconductivity measurements were performed to investigate the interface states at amorphous CHO/STO interfaces. Understanding the nature of interface states is important because such in-gap states can degrade the performance of amorphous CHO/STO FETs at low temperatures.

The interface states could not be observed directly in optical absorption measurements because the interface layer is too thin to be detected by transmittance and reflectance measurements.

In photoconductivity measurements, an oxygen vacancy-related peak was observed at around 2.3 eV from the conduction band bottom of STO in amorphous CHO/STO heterostructures. STO substrates and amorphous CHO films grown on other insulating substrates did not show such a photoconductivity peak structure. Therefore, it can be concluded that this peak is characteristic of STO interfaces only. And annealing treatment showed that the origin of the photoconductivity peak at 2.3 eV is in the formation of oxygen vacancies in the STO surface layer. Other experiments have shown that the density of such surface defects depends on the ablation laser energy density, and thus the flux and kinetic energy of the ions and atoms hitting the substrate surface at the initial stage of film growth. It appears that oxygen vacancies are caused by the sputtering effect of the ablation plume during insulator layer deposition. Applying an annealing treatment at 300 °C for 6 hours in air, caused the main oxygen vacancies-related peak to disappear. However, although this treatment was done in the process of amorphous CHO/STO FET fabrication, the transistor performance still degraded upon cooling. Therefore, the oxygen vacancy photoconductivity peak observed in this study is not the only reason for carrier trapping at STO interfaces.

References

[1] O.N.Tufte, P.W.Chapman

Electron mobility in semiconducting Strontium Titanate

Phys. Rev. 155, 796 (1967)

[2] T.Hasegawa, M.shirai, K.Tanaka

Localizing nature of photo-excited states in $SrTiO_3$

J.Luminescence. 8, 1217 (2000)

[3] K.Shibuya, T.Ohnishi, M.Lippmaa, M.Kawasaki, H.Koinuma

Domain structure of epitaxial $CaHfO_3$ gate insulator films on $SrTiO_3$

Appl.Phys.Lett. 84, 2142 (2004)

[4] W.Marti, P.Fischer, F.Altorfer, HJ.Scheel, M.Tadin

Crystal structure and phase transition of orthorhombic and rhombohedral $RGaO_3$ (R=La,Pr,Nd) investigated by neutron powder diffraction

J.Phys:Cond.Matt. 6, 127 (1994)

[5] W.S.Baer

Free-Carrier Absorption in Reduced $SrTiO_3$

Phys.Rev. 144, 734 (1966)

[6] S.Mochizuki, S.Minami, F.Fujishiro

The reversible UV-laser-light-induced spectral change and origin of the 2.4 eV luminescence band in $SrTiO_3$

J.Luminescence. 112, 267 (2005)